ROYAL SOCIETY OF CHEMISTRY

Check for updates

Photoelectrochemical conversion of glycerol aqueous solution to value-added chemicals using $Bi_2Fe_4O_9$ as a photoanode†

Bruno L. da Silva, [a] Saulo A. Carminati, [b] Matheus B. C. Souza,[a] Leonardo C. Soares, [a] Claudia Longo,[a] Pablo S. Fernández [a] and Ana F. Nogueira ⋆[a]

A low-cost, stable and non-toxic $Bi_2Fe_4O_9$ (BFO) photoanode was used for the first time to promote glycerol aqueous solution photoelectrochemical conversion to hydrogen and value-added chemicals. Photoelectrochemical measurements were performed under AM1.5G irradiation using a three-electrode cell. The best performance was achieved in alkaline medium, where four distinct glycerol oxidation products were detected (glycerate, formate, glycolate and lactate). In neutral medium, no oxidation products were detected. In acidic medium, we observed an improved selectivity, with only glyceraldehyde and dihydroxyacetone as oxidation products. Our results show that the electron–hole recombination, which restricts the efficiency of glycerol conversion, is one of the main shortcomings of BFO. However, its high open circuit potential (OCP) value and several other desirable properties for a good photoelectrocatalyst make it a material worth further research.

1 Introduction

The replacement of the oxygen evolution reaction (OER) in the water splitting process by biomass derivatives is considered a favorable approach for clean hydrogen generation. This strategy enables the simultaneous production of value-added biomass-derived chemicals and green hydrogen. Besides, the substitution of the OER by the oxidation of organic molecules usually includes an energy saving, due to the lower electrochemical potentials required for the oxidation of organic molecules.[1,2]

Brazil is the third largest producer of biodiesel (6.76 million m^3) in the world.[3] This high production and demand have also increased the availability of glycerol (Gly), which is one of the by-products of biodiesel production. This huge volume of Gly largely surpasses the demand, making it urgent to find new uses for this compound or increase its value.

Gly has many oxidation products, like 1,3-dihydroxyacetone (DHA), formic acid (FA), glycolic acid (GA), glyceric acid (GLA), glyceraldehyde (GLAD), etc. Valuable products such as DHA, GLA and GLAD can be obtained through thermal or electrochemical Gly oxidation on noble metal-based electro-catalysts, like Pt, Au and Pd. However, in addition to this process being cost-intensive, the selectivity and production rate of these products are still not satisfactory.[4–6]

Low-cost metal oxides, which are abundant, versatile, and non-toxic, can be excellent alternative materials for this process. In this context, bismuth-based ferroelectric oxides like $Bi_2Fe_4O_9$ (BFO), $BiFeO_3$ and $Bi_{25}FeO_{40}$, which possess a suitable bandgap for solar energy harvesting, are considered promising photo-catalysts for applications in solar energy conversion.[7–9]

$Bi_2Fe_4O_9$ is categorized as mullite, and its crystal system type is orthorhombic (Pbam space group). BFO was introduced in the 1990s, like the other two bismuth ferrites (perovskite $BiFeO_3$ and selenite $Bi_{25}FeO_{40}$), as a potential material for application in gas sensors. Following this, its potential has been investigated in other approaches, namely as a catalyst for ammonia oxidation and photocatalytic applications.[10]

When compared to $BiFeO_3$, $Bi_2Fe_4O_9$ is much less well-studied. Recently, mullite-type bismuth ferrite was used for the first time in its pure phase as a photoanode for photoelectrochemical water oxidation.[11] Despite not showing outstanding activity yet, the material presented excellent stability, which is likely the main barrier for the industrial application of solar energy-driven photoelectrochemical (PEC) water splitting, making this material a promising candidate.

In this work, we propose to use $Bi_2Fe_4O_9$ as a photoanode to promote the photoelectrochemical conversion of aqueous Gly solutions to simultaneously produce value-added chemicals and clean hydrogen. The aim of this work is to answer the

[a]Laboratório de Nanotecnologia e Energia Solar, Instituto de Química, Universidade Estadual de Campinas, 13083-970 Campinas, SP, Brazil. E-mail: anafla@unicamp.br

[b]Instituto de Pesquisas Energéticas e Nucleares, IPEN/CNEN, Av. Prof. Lineu Prestes, 2242-Cidade Universitária, São Paulo, SP, 05508-000, Brazil

following questions: is BFO able to carry out the photo-electrooxidation of glycerol? What is the best working pH condition? How does pH affect the kinetics and selectivity of reactions? What is the main drawback of BFO and how can we improve it?

By performing experiments in conventional three-electrode H-cells, we found higher values of photocurrent (at 1.23 V vs. RHE) in alkaline media, more than one order of magnitude compared to pH = 5.5 and pH = 3.5. In terms of hydrogen generation (the BFO photoanode limits the system's efficiency and, therefore, the oxidation current is equal to the reduction current at the Pt cathode, leading to the correspondent formation of hydrogen), we observed a higher amount of hydrogen produced at pH 13.0, followed by pH 5.5 and pH 3.5.

Regarding the reaction selectivity, we found that in alkaline media, glycerate, glycolate, lactate and formate were produced through glycerol PEC oxidation. At a pH of 3.5, a higher selectivity was achieved, producing only DHA and GLAD. Lastly, at a pH of 5.5, no products of glycerol PEC oxidation were detected.

To explain the activity trend observed (pH 13 > pH 3.5 > pH 5.5) we combined some techniques like transient absorption spectroscopy (TAS), open circuit potential decay (OCPD) and electrochemical impedance spectroscopy (EIS) and observed that the activity can be limited to the lifetime of photogenerated electrons and holes.

2 Experimental

2.1 Materials and methods

All materials were used without any previous treatment: bismuth(III) nitrate (Bi(NO$_3$)$_3$·5H$_2$O ≥98.0%, Sigma-Aldrich®), iron(III) nitrate (Fe(NO$_3$)$_3$·9H$_2$O, ≥98.0%, Sigma–Aldrich®), 2-methoxyethanol (C$_3$H$_8$O$_2$ ≥99.9%, Sigma-Aldrich®), acetic anhydride (C$_2$H$_6$O$_3$ ≥99%, Sigma-Aldrich®), 1.1 mm thick aluminoborosilicate glass substrate with 10 Ω sq^{-1} fluorine doped tin oxide.

2.1.1 Bi$_2$Fe$_4$O$_9$ (BFO) photoanode preparation. Bi$_2$Fe$_4$O$_9$ photoanodes were prepared by the chemical solution deposit method (CSD) on fluorine doped tin oxide glass (TCO10-10 Solaronix).[11] The substrates were cleaned by bath sonication (for 20 min) in methanol, acetone, isopropyl alcohol and Milli-Q water, respectively. After sonication, the substrates were treated by ultraviolet ozonation for 30 min. The precursor solution was prepared with a Bi : Fe ratio of 1 : 2, dissolving 4 g of bismuth nitrate and 6 g of iron nitrate in 20 mL of 2-methoxyethanol. Acetic anhydride (10 mL) was then added under constant stirring to form BFO precursor solution.

Thin films were prepared by adding 80 μL of precursor solution onto the substrate and then, the films were spin-coated at 3000 rpm for 1 min at a rate of 1500 rpm s^{-1}. The as-deposited films were heated on a hot plate at 90 °C for 1 min and then at 350 °C for 5 min, followed by transfer to a tube furnace and heated at a rate of 5 °C min^{-1} to 450 °C with a dwell time of 30 min before a second heating to 700 °C at 5 °C min^{-1}, and held for 1 h. The annealing processes were conducted under an oxygen atmosphere and samples were then cooled to

room temperature within the furnace. In order to achieve thicker films, the deposition process was repeated 5 times.

2.1.2 BFO photoanode characterization. The electrodes were characterized by X-ray diffraction (XRD) using an X-ray diffractometer XRD-7000 of Shimadzu with a voltage/current of 40 kV/30 mA, a scanning angle of 2θ from 10° to 70° and a scan speed of 2° min^{-1}. The morphology of the as-prepared BFO was obtained by field emission-scanning electron microscopy (Quanta 250 FEG-SEM). UV-vis spectra were recorded on an Agilent Cary 60 UV-vis. To analyse the chemical composition and the oxidation states of elements present in the BFO photoelectrode, X-ray photoelectron spectroscopy (XPS) analysis was carried out using a Thermo Scientific instrument (K-ALPHA), utilizing Al Kα radiation. The XPS high-resolution spectra were recorded at a constant pass energy of 50 eV with a 0.02 eV per step.

2.1.3 Photoelectrochemical (PEC) characterization. PEC studies were carried out in a double compartment, homemade photoelectrochemical cell, in a three-electrode configuration with BFO as the working electrode, Pt foil as the counter electrode and Ag/AgCl (KCl 3 mol L^{-1}) as the reference electrode. Chambers are separated with a Nafion perfluorinated membrane to avoid the crossover of the photoelectrochemical products. The measurements were obtained under irradiation with a polychromatic light under an intensity of 100 mW cm^{-2} (450 W Xenon lamp, AM 1.5G).

PEC measurements were carried out using a potentiostat/galvanostat (μAutolab III) and scan rates of 10 mV s^{-1} were employed for current density measurements. The illuminated area of the BFO working electrodes was approximately 1 cm^2. The electrolytes used were: 0.1M NaOH for alkaline pH (pH = 13), 0.3 mM H$_2$SO$_4$ for acidic pH (pH 3.5) and 0.2 M Na$_2$SO$_4$ for pH 5.5.

The Ag/AgCl electrode potential was converted to the RHE by using the Nernst equation, as shown in eqn (1):

$$E_{RHE} = E_{Ag/AgCl} + 0.059 \, pH + E_{Ag/AgCl^0} \tag{1}$$

where E_{RHE} is the potential vs. RHE, $E_{Ag/AgCl}$ is the potential vs. Ag/AgCl and $E_{Ag/AgCl(KCl \, 3M)^0}$=0.210 V at 25 °C.

The electron lifetime recombination was estimated from open circuit potential decay (OCPD) through the slope value dV_{oc}/dt appearing after the illumination is turned off and was estimated according to eqn (2).

$$\tau = \frac{kT}{e} \left(\frac{dV_{oc}}{dt} \right)^{-1} \tag{2}$$

where k, T, and e are Boltzmann's constant, temperature in K, and elementary electron charge, respectively.

Electrochemical impedance spectroscopy (EIS) was performed using the same three-electrode cell. The spectra were collected in a frequency range of 0.1–10^4 Hz with an amplitude of 10 mV, from 0.66 V to 1.23 V vs. RHE.

The incident photon-to-current conversion efficiency (IPCE) values were obtained according to eqn (3):

$$IPCE (\lambda) = (J1240/P_{light}\lambda) \tag{3}$$

where J is the measured photocurrent density (mA cm^{-2}), 1240 is the value obtained by multiplying Planck's constant (h) by the speed of light (c), P_{light} is the monochromatic illumination power (mW cm^{-2}) and λ is the wavelength (nm) of the incident light. These measurements were carried out using a Metrohm potentiostat (PGSTAT 302N/FRA32) and ThorLabs optical devices in a 0.1M NaOH and 0.1M NaOH + 0.1M Gly electrolyte at 1.23 V *vs.* RHE.

The selectivity of Gly oxidation products was calculated based on eqn (4):

$$\text{Selectivity} = \frac{c_{\text{oxidation product analized}}}{c_{\text{all}}} \quad (4)$$

where c is the product concentration detected by high-performance liquid chromatography (HPLC) and c_{all} is the sum of all products generated at their respective pH values.

2.1.4 Transient absorption spectroscopy (TAS). TAS measurements on the μs-s time scale were obtained using a pump-probe transient absorption spectrometer (Optical Building Blocks Corporation – OBB). A nitrogen laser was used as the UV excitation source (337 nm, pulse width = 6 ns, 150 μJ cm^{-2} pulse^{-1}, and typically 1 Hz repetition). The probe pulse was obtained using a light source (tungsten lamp) with two OBB monochromators. The transient decay data are the result of averaging between 100 and 300 laser shots.

The studies were conducted in a quartz cuvette filled with electrolyte solution (0.2 M Na$_2$SO$_4$) in the presence and absence of Gly (0.1 M). For measurements with the application of an external electric bias, a Pt wire was used as the counter electrode, Ag/AgCl (saturated KCl 3 mol L^{-1}) as the reference electrode and BFO as the working electrode.

2.1.5 High-performance liquid chromatography (HPLC). HPLC measurements were performed using a Shimadzu LC-6AD chromatograph with a quaternary pump, a thermostatic column compartment, a UV-vis and a refractive index (RID) detector, both kept at 35 °C. Three columns (one Aminex HPX-87H and two Shodex Sugar SH1011) were used in series with a Bio-Rad 1250131 precolumn, kept at 84 °C. The mobile phase was 0.5 mM H$_2$SO$_4$ with a flow rate of 0.6 mL min^{-1}, and the injection volume was 20 μL.

2.1.6 Gas chromatography (GC). The accumulation of hydrogen in the counter electrode compartment was measured every two hours for a total of ten hours of reaction *via* gas chromatography on an HP 6890 gas chromatograph equipped with a thermal conductivity detector and Agilent CarboPLOT P7 column using N$_2$ as the carrier gas.

3 Results and discussion

3.1 Bi$_2$Fe$_4$O$_9$ (BFO) photoelectrode characterization

During the synthesis of bismuth ferrite (both perovskite and mullite-type bismuth ferrite), it is very common to observe the formation of secondary phases. While the phases Bi$_2$O$_3$, Bi$_2$Fe$_4$O$_9$ and Bi$_{25}$FeO$_{39}$, are common to be observed during perovskite formation,[12,13] phases such as BiFeO$_3$, Fe$_2$O$_3$ and Bi$_{25}$FeO$_{39}$ can be observed during mullite synthesis.[14–16] The appearance of these secondary phases in perovskite can be related to the kinetics of phase formation and the high volatility of bismuth.[17,18]

To confirm that the mullite was synthesized in its pure phase, X-ray diffraction was performed, as shown in Fig. 1a. The diffraction pattern confirms that pure phase Bi$_2$Fe$_4$O$_9$ was synthesized with an orthorhombic structure (CIF 9008148), lattice constants of $a = 7.905$ Å, $b = 8.428$ Å, and $c = 6.005$ Å and space group *Pbam*. All additional peaks can be assigned to the fluorine-doped tin oxide glass (FTO) substrate.

The morphology of the Bi$_2$Fe$_4$O$_9$ film was characterized using SEM, as shown in Fig. 1b and c. The film is composed of grains ranging from 85 to 150 nm. In the higher magnification image (Fig. 1c), it is evident that the film is formed by small crystallites. A Bi$_2$Fe$_4$O$_9$ film thickness of 560 nm was estimated through a cross-section image, as shown in Fig. 1d. The film thickness was measured in three different regions, with no significant variation between them.

To further investigate the formation of Bi$_2$Fe$_4$O$_9$, EDX analysis was performed in three different regions of the sample and the results are in good agreement with XRD data, confirming that we were successful in obtaining a pure phase of mullite. The details of these regions measured in atomic and weight percentages are listed in Table S1.† The EDX spectra are shown in Fig. S1.†

To gain insights into the valence states and surface defects on BFO films, X-ray photoelectron spectroscopy (XPS) was carried out and the results are shown in Fig. 1e–g. The obtained binding energies were normalized by referencing the C 1s line to 284.6 eV.

The survey XPS spectrum (Fig. S2†) shows that only Bi, Fe and O elements are present in the sample. In the Fe XPS spectrum (Fig. 1e) we observe the presence of two Fe peaks located at 710.16 eV and 723.68 eV corresponding to Fe 2p$_{3/2}$ and Fe 2p$_{1/2}$, respectively. The peaks at 718.28 eV and 732.83 eV correspond to the Fe 2p$_{3/2}$ and Fe 2p$_{1/2}$ satellite peaks, respectively. Thus, it can be confirmed that Fe is in the 3+ valence state.[19,20]

The O 1s line can be deconvoluted into two different peaks corresponding to 529.50 eV and 531.70 eV. Due to the *ex situ* nature of this analysis, the BFO photoelectrode was exposed to ambient water vapor, which has healed any possible oxygen vacancies and contributes to the O1s signal. This signal, observed at 531.70 eV, is associated with the surface hydroxyls, formed upon dissociatively adsorbed water molecules.[21] The peak in lower binding energy (529.50 eV) corresponds to M–O–M bonds.

Fig. 1g shows the XPS spectrum of Bi 4f. The Bi peaks at 158.81 eV and 164.10 eV reveal the presence of bismuth in its 3+ oxidation state, as expected for the Bi$_2$Fe$_4$O$_9$ mullite structure.

The optical absorption of the Bi$_2$Fe$_4$O$_9$ thin films was measured using UV-vis spectroscopy. As shown in Fig. S3a,† BFO thin films exhibited good light absorption along the UV-visible region, which is a desirable feature of a photoelectrocatalyst. A broad peak was observed from 610 nm to 760 nm and may be ascribed to the Fe^{3+} d–d transitions, derived from the splitting of the Fe 3d orbital into Fe t$_{2g}$ and Fe e$_g$.[8,22] The same peak was observed in Bi$_2$Fe$_4$O$_9$ nanoparticles synthesized by a hydrothermal method.[7,23] Based on UV-vis
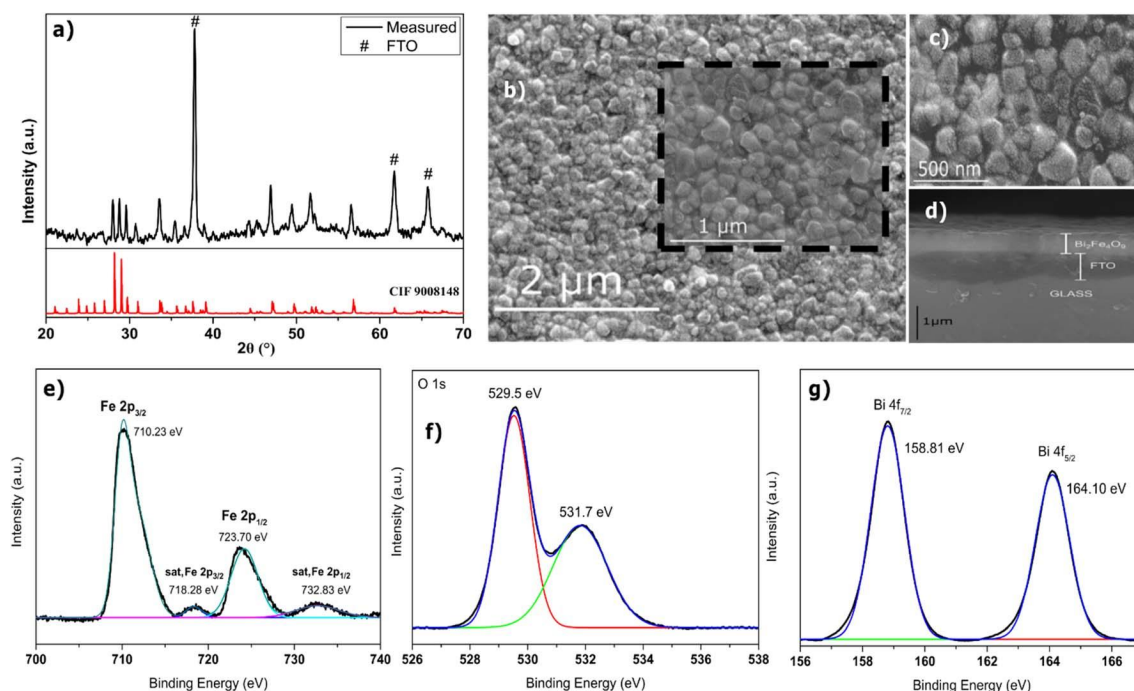
Fig. 1 BFO photoelectrode characterization: (a) XRD pattern of the FTO|BFO thin film (# indicates FTO substrate peaks). (b and c) Top-view SEM images of the FTO|BFO film and (d) cross-sectional view. XPS spectrum of the FTO|BFO film with fitted peaks: (e) Fe 2p, (f) Bi 4f and (g) O 1s.

measurements, the band gap was calculated through a Tauc plot (Fig. S3b†) and it was estimated to be 2.08 eV for the allowed direct and 2.86 eV for the allowed indirect band gap.

3.2 PEC performance of the Bi₂Fe₄O₉ photoelectrode

Depending on the thickness of the films, higher efficiency values (in terms of photocurrent) can be achieved by illuminating the electrodes from the front or back side.[24] Some studies using α-Fe₂O₃ electrodes show that thicker films exhibit greater values of photocurrent when illuminated from the back side, while thinner films reveal higher photocurrent values when the front side is illuminated.[25]

The PEC activity of the BFO photoanode was first evaluated by verifying which side of the electrode should be illuminated to achieve higher photocurrents. The difference in photocurrent under front-side (Bi₂Fe₄O₉ side) and back-side (FTO side) illumination was evaluated by linear sweep voltammetry (LSV) and the values obtained at 1.23 V *vs.* RHE and 1 sun (100 mW cm²), at different pHs are shown in Fig. S4.† A schematic illustration of the electrode irradiation side is shown in Fig. S5.† Higher photocurrents were achieved by illuminating the electrode from the front side in the whole pH range, indicating that holes can be efficiently extracted by directly illuminating from the Bi₂Fe₄O₉ side. Therefore, all measurements in this work were performed using front-side illumination.

Fig. S6† shows the *J–V* profiles under dark and illumination conditions for the oxygen evolution reaction (OER) and glycerol oxidation reaction (GOR). Under dark conditions, we did not observe faradaic current in the potential window measured (from 0 V to 1.4 V *vs.* RHE). Under illumination, PEC water oxidation (in the absence of glycerol) was observed at all the

pHs, showing higher activities at pH 13, followed by pH 3.5 and pH 5.5.

A similar trend was observed when glycerol was added to the reaction medium and the photocurrent (at 1.23 V *vs.* RHE) increased from 33 to 193 μA cm⁻², from 23 to 44 μA cm⁻² and from 12 to 25 μA cm⁻² under alkaline (pH 13), acidic (pH 3.5) and neutral (pH 5.5) conditions, respectively. In addition to this increase in the photocurrent values, the oxidation onset shifted towards lower potentials after glycerol addition, indicating that the oxidation of glycerol occurs preferentially to water.

The highest activities in alkaline media suggest that the presence of hydroxyl ions could somehow improve the catalytic oxidation reaction for BFO photoanodes. However, at this pH, the increase in photocurrent density (in the presence of glycerol, from 0.5 V to 1.4 V) is consistent with the fact that the addition of glycerol considerably increases the IPCE throughout the BFO light absorption region, as shown in Fig. S7.†

LSV was also used to estimate the flat band potential (E_{FB}) for the BFO photoanode. Since the Fermi energy level and the position of the conduction band edge can be related to the flat band potential, it is an important metric for understanding the photoelectrochemical properties of a semiconductor electrode.[26]

Its value is highly influenced by the medium conditions, including pH, electrolyte composition, and the semiconductor crystalline structure, as well as morphology and film thickness. The E_{FB} value for alkaline medium in the presence and absence of glycerol was estimated through the Butler–Gartner model as shown in Fig. S8† and the values obtained were 0.68 V for the GOR and 0.92 V for the OER.

To verify the stability of the BFO photoanodes, chronoamperometry measurements at 1.23 V *vs.* RHE in the presence of glycerol were carried out. The photoanodes demonstrated a pronounced increase in photocurrent over time for alkaline pH (from 37 to 214 $\mu A\ cm^{-2}$), possibly due to the surface hydroxylation, stabilizing at the eighth hour of measurement, as shown in Fig. S9a†.

Following the measurements of chronoamperometry with glycerol, we also evaluate the stability of the BFO photoanodes for water oxidation. BFO photoelectrodes were stable for water oxidation, since the photoelectrodes were able to maintain up to 95% of their initial photocurrent after 2 h at all analyzed pH, as shown in Fig. S9b.†

To further verify the stability of the photoelectrode across the potential sweep, we performed cyclic voltammetry measurements (3 cycles), as shown in Fig. S10.† The electrode was stable from 0 V to 1.4 V *vs.* RHE at all measured pH values and no BFO oxidation/reduction peaks were observed.

Fig. 2 shows the chopped LSV profiles in the absence and presence of glycerol. At pH 3.5, the on–off cycle produces a transient spike at potentials lower than 1.2 V *vs.* RHE, while at pH 5.5 we observed these spikes even higher and throughout the entire applied potential range.

The transient photocurrents (spikes observed in chopped-light measurements) are associated with the extraction of holes and electrons under non-equilibrium conditions and herein, were ascribed to hole accumulation at the photoanode/electrolyte interface.[4,27] If these charges are not effectively separated, they may recombine, resulting in an efficiency loss.

The photopotential of BFO photoelectrodes was investigated according to pH in the presence and absence of glycerol by open circuit potential (OCP) experiments. The results are shown in Fig. S11 and Table S2.†

To better understand the influence of pH and glycerol on the recombination kinetics of BFO photoelectrodes, we focus on the potential relaxation region right after the illumination is turned off in OCP measurements.

The recombination process is expressed by the "electron lifetime" (τ), which represents an average survival time for the electrons accumulated at the oxide.[28] Fig. 3a shows the τ values obtained from open circuit potential decay (OCPD).

When glycerol was added to the solution, we observe the appearance of a long-lived signal, which is indicative of long-lived charges that avoided rapid recombination.

To further investigate the reaction kinetics, the dynamics of the photogenerated charges were investigated by transient absorption spectroscopy (TAS) from microsecond to second timescales. This technique employs low excitation densities compared to ultrafast spectroscopy and is more adequate to study sluggish reactions like the OER.[29]

Fig. 3b shows the transient absorption spectra of BFO films in 0.2M Na_2SO_4 (pH 5.5) probed from 550 nm to 800 nm and recorded in 10 μs after the laser excitation. The negative value of ΔOD refers to a ground state bleach, as BFO absorbs at 550 nm. From 600 nm onwards, we observe a photo-induced absorbance (positive values of ΔOD in the spectrum). The highest ΔOD value was observed at 700 nm and all the subsequent measurements were probed at this wavelength. The transient signal at this wavelength was assigned to photogenerated BFO electrons as discussed below.

The red curve in Fig. 3c shows the transient absorption decay of the BFO film in 0.2M Na_2SO_4 solution. Some studies report
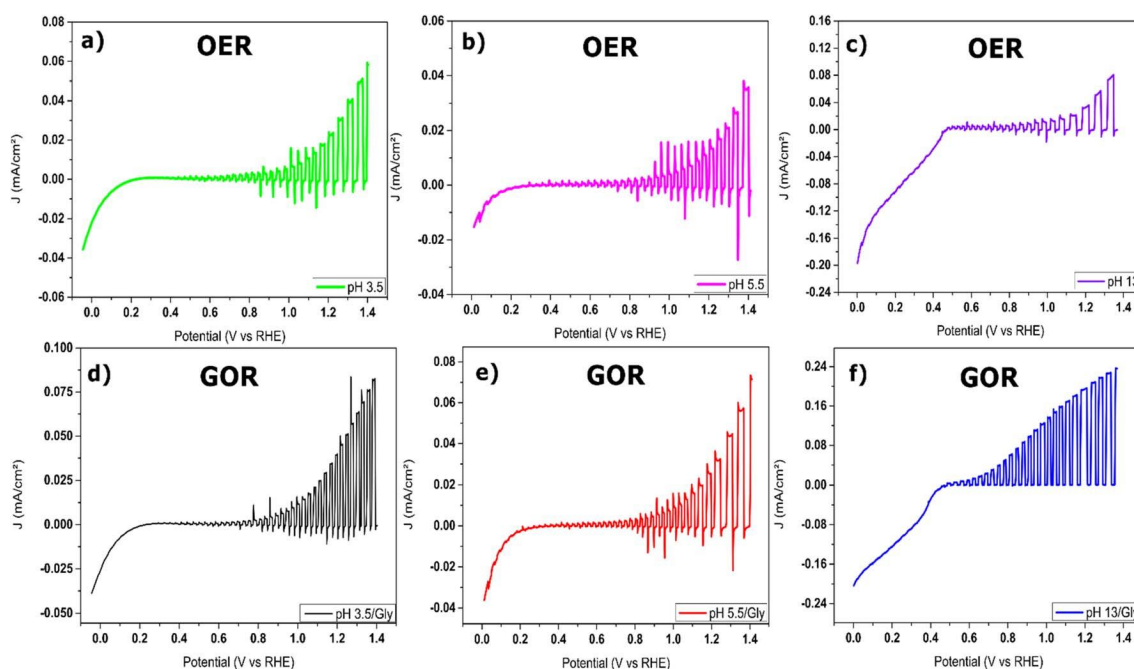

Fig. 2   Linear sweep voltammetry using FTO|BFO as the photoanode under chopped irradiation (AM 1.5G). (a) pH 3.5 OER, (b) pH 5.5 OER, (c) pH 13.0 OER, (d) pH 3.5 GOR, (e) pH 5.5 GOR and (f) pH 13.0 GOR.
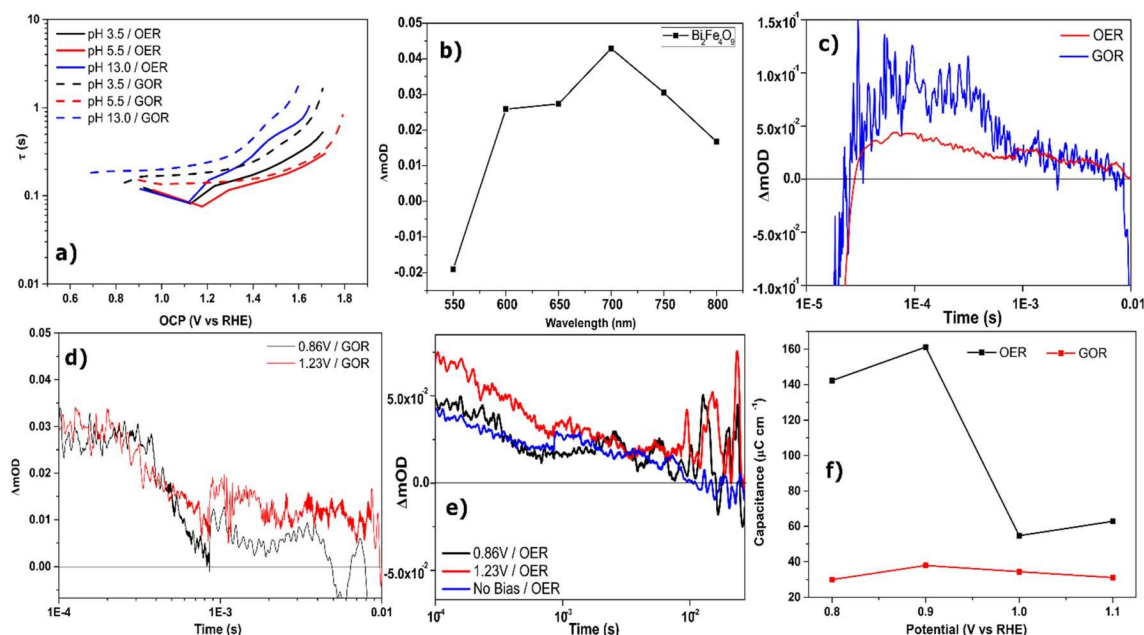
Fig. 3 FTO|BFO photoelectrochemical properties: (a) electron lifetime from OCPD for the OER and GOR, (b) transient absorption spectra in 0.2M Na_2SO_4 recorded 10 μs after the laser excitation, (c) transient absorption decay of the BFO film probed at 700 nm in the presence and absence of glycerol, (d) effect of electrical bias on transient absorption decay for the OER, (e) effect of electrical bias on transient absorption decay for the GOR and (f) double-layer capacitance values at pH 13.

that water is oxidized on the timescale of microseconds to seconds,[29,30] and therefore the decay observed before this time may be associated with the recombination of photogenerated electron–hole pairs.

When glycerol (hole acceptor) was introduced into the solution, we observed a biphasic decay (blue curve). At early times (<1 ms), a fast decay is observed and should be assigned to the alcohol oxidation, suggesting that the surface oxidation kinetics determines the transient lifetime. The slower decay observed on the millisecond-to-second timescale (>1 ms) evidences that the water oxidation still occurs even in the presence of glycerol, since the red (OER) and blue (GOR) curves have the same intensity on this timescale.

Besides that, the faster kinetics in the presence of glycerol also indicates that its oxidation occurs preferentially compared to water. This observation agrees with other studies that show that the photocatalytic oxidation rate of alcohols, like methanol, ethanol and propanol, is much faster than that of water.[31,32]

Furthermore, the increase of the ΔOD in the presence of glycerol at this wavelength supports the association of the transient signal with photogenerated electrons.

We also evaluated the effect of an external electrical bias on the transient absorption decays, as can be seen in Fig. 3d and e. Both for the OER and GOR, we observe longer-lived carriers when bias was applied. The highest increase in the lifetime of photogenerated electrons was observed at 1.23 V vs. RHE. These results reveal the importance of the external bias applied in BFO photoanodes. The positive bias generates long-lived charges, which are responsible for driving the surface oxidation/reduction reactions.

To better understand the charge transfer and recombination processes in BFO photoelectrodes, we compared electrochemical impedance spectroscopy (EIS) measured in the dark and under light with different applied biases in the presence and absence of glycerol.

To determine the resistance and capacitance values for the OER and GOR in alkaline medium from the impedance data, we used an equivalent circuit indicated in Fig. S12.† The values obtained are shown in Tables 3 (OER) and 4 (GOR) and represented in Fig. S13.† The Nyquist plot in the potential range used for calculating these parameters is shown Fig. S14.†

From the Bode plots shown in Fig. S15 and S16,† we observe that under dark conditions, the electrode has a capacitive-like behaviour in the potential window measured, which explains the very low faradaic current observed in voltammetry. This behaviour was also confirmed by the Nyquist plots (Fig. S17 and S18†), where we observe that there was no actual charge transfer in the dark, regardless of the applied bias and the pH.

However, during illumination, from 0.86 V onwards, the electrode began to exhibit characteristics of a charge transfer controlled reaction, which increases according to the applied potential. We note that an increase in the applied bias led to a frequency peak decrease in the Bode plot and a shift toward high frequency, leading to a decrease in faradaic resistance and improving the surface reaction rate.

According to the impedance modulus (Fig. S19†), the increase in the electrical bias applied leads to a decrease in the overall impedance at pH 3.5 and 5.5, suggesting that the increase in the electrical bias still contributes to a decrease in the faradaic resistance, facilitating the chemical reactions. It

can also be verified through the phase decrease in the low-frequency region in the Bode plot (Fig. S15 and S16†) and the decrease in the charge transfer resistance in the Nyquist plot (Fig. S17 and S18†).

However, for alkaline pH, the increase in electrical bias to values greater than 0.86 V (in the presence of glycerol) no longer causes significant variations in the system impedance, indicating that, under these conditions, the reaction is limited by a step/process that is not improved by applying additional bias. At this pH, we also observed a considerable decrease in the charge transfer resistance (R_{CT}) when glycerol is introduced into the electrolyte, which explains the increase in the current values at lower potentials observed in voltammetry.

3.3 PEC performance: general discussion

Both linear sweep voltammetry and chronoamperometry experiments showed that the activity of BFO is higher in the presence of glycerol and follows the trend pH = 13, 3.5 and 5.5. Besides, linear sweep voltammetry under chopped irradiation shows the presence of spikes, suggesting hole–electron recombination, explaining one of the main factors that limit the material's activity. To understand these observations more in detail, we performed OCPD, TAS and EIS.

OCPD showed that the recombination occurs faster at pH 5.5, followed by pH 3.5 and 13, respectively. This observation agrees with the LSV measurements both in the absence and the presence of glycerol, suggesting that the charge recombination process can be the limiting factor to achieve higher photocurrent.

TAS measurements complemented OCPD results showing that glycerol oxidized faster than water, avoiding the recombination of some holes accumulated at the BFO surface. Furthermore, TAS also demonstrated that the lifetime of photogenerated charges increases at higher applied electrical bias, increasing the probability of glycerol/water oxidation.

The fundamental cause of recombination in $Bi_2Fe_4O_9$ photoelectrodes is that this material is a multiband semiconductor and exhibits a middle narrow energy band between the valence and conduction bands.[22] This middle band may act as a center for charge recombination, which would reduce the efficiency of the photocatalyst. However, this middle band is not strongly localized, and the recombination can be minimized by using different approaches such as applying an electrical field, adding electron or hole scavengers, etc.[22,33]

As observed in this study, the transient photocurrent was remarkably reduced (pH 3.5 and 5.5) or even suppressed (pH 13.0) by the addition of glycerol or by the application of a sufficient anodic potential. In terms of electric bias applied, this phenomenon can be explained through the magnitude of band bending. Under small and moderate applied potentials, the band bending is insufficient, which increases the chances of electron–hole recombination both in the surface and in the bulk of the photocatalyst.[27]

Regarding the effect of glycerol on decreasing the transient photocurrents, due to its faster oxidation kinetics compared to water oxidation, it is capable of promoting the reaction of

accumulated holes at the interface of BFO/electrolyte and suppressing back electron–hole recombination.

The results described before show that in alkaline medium, the photogenerated carriers are better separated, reducing the charge recombination. The surface hydroxylation of the BFO photoelectrode that takes place at this pH may be a key factor to explain this observation, since the surface hydroxyl groups can act as a hole collection layer,[34] mediating the transfer of photoinduced holes and resulting in the better performance observed.

By far, the most studied semiconductor for PEC applications is α-Fe_2O_3 (hematite). Many literature reports show that hematite faced similar problems to BFO, and the performance of hematite-based photoanodes has been improved during the last few decades by: improving photogenerated charge separation (i.e., doping and heterojunction), lowering the overpotential (through a surface passivation layer and cocatalyst loading), constructing nanostructured electrodes and controlling the film thickness.[35]

Therefore, precious time can be saved by following the same strategy with BFO to rapidly improve the current density of a material that has shown excellent stability and could theoretically attain higher currents than hematite (over 15 mA cm^{-2}).[36]

3.4 The reaction selectivity and the generation of valuable chemicals

To verify the influence of pH on the selectivity of the reaction on our photoanodes, we collected samples during 10 h of glycerol oxidation at 1.23 V vs. RHE under illumination. The product concentration and selectivity are shown in Fig. 4 for alkaline and acidic conditions.

In alkaline media, the main products were glycerate, glycolate, lactate, and formate. While glycolate concentration remains almost constant during the 10 hours, glycerate, lactate and formate grow linearly. Lactate is not directly produced by an electrochemical reaction but can be produced through the Cannizaro reaction of two molecules in equilibrium with DHA in alkaline media.[37,38] The production of DHA makes it likely that some of the glycerate produced comes not only from electrochemical oxidation but also, again, from the chemical disproportion of glyceraldehyde.[39]

Interestingly, we observe a much higher concentration of glycolate (C_2 product) than formate (C_1 product). However, if glycerol is oxidized to glycolate, which has 2 carbons in its structure, a molecule with one carbon must be formed, suggesting that carbonate (CO_3^{2-}) was also formed during the reaction. The assignment of the C_1 molecule to carbonate is due to the alkaline medium. At that pH, the production of carbonate is expected instead of CO_2 in the bulk solution.[40] The presence of formate indicates that the BFO photoanode is capable of completely breaking the C–C chain of glycerol.

Under acidic conditions, only GLAD and DHA were detected as oxidation products, with the latter having a higher selectivity. At this pH, our photoelectrode exhibits lower photocurrent (at 1.23 V vs. RHE) compared to pH 13. At pH 5.5, despite the higher
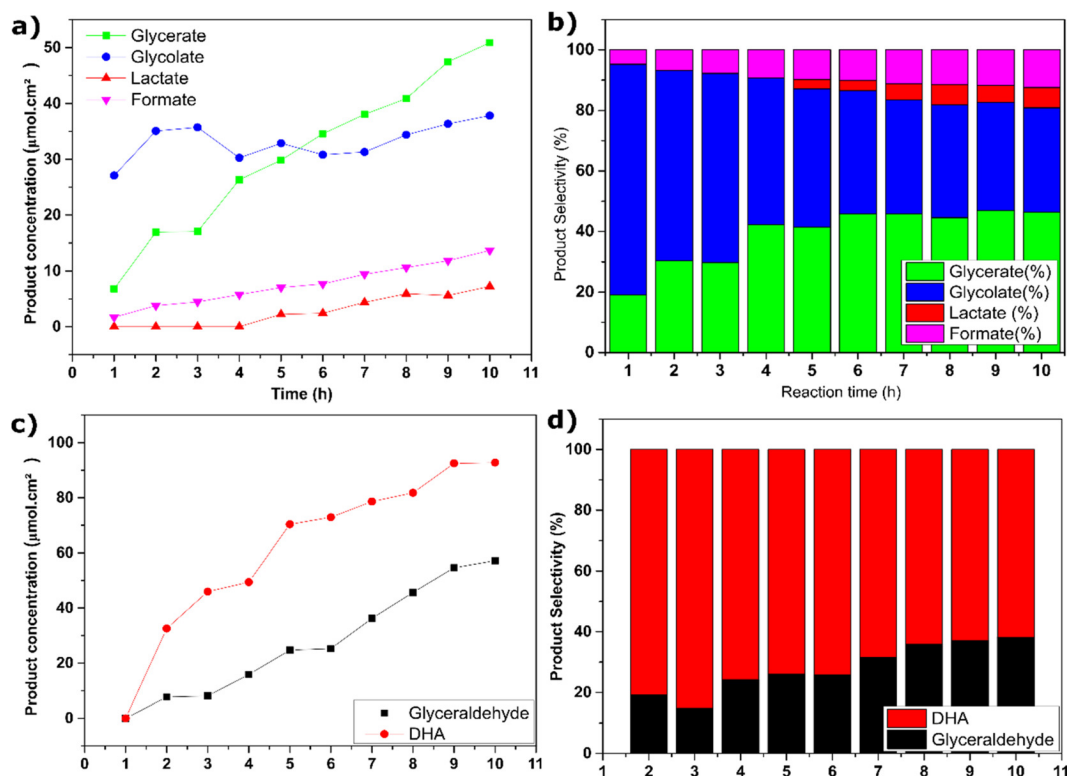
Fig. 4 Product concentration and selectivity of glycerol photoelectrochemical oxidation on FTO|BFO photoanodes in (a and b) alkaline medium and (c and d) acidic medium.

photocurrent exhibited in the presence of glycerol, the photocurrent is still very low and the possible products formed were not detected by HPLC.

The hydrogen gas generated at the Pt cathode was quantified by GC and its concentration with time is shown in Fig. 5. As the photoelectrode exhibits much higher photocurrent at 1.23 V *vs.* RHE in alkaline media, we expected a higher amount of hydrogen observed at this pH.

In alkaline medium, we observed 1.19 μmol of hydrogen produced in the tenth hour of chronoamperometry, while for pH 3.5 we observed 0.085 μmol. At pH 5.5, hydrogen gas was not detected. Probably, at this pH, due to the low photocurrent observed, the hydrogen generated was below the GC detection limit. In terms of hydrogen generation, alkaline medium proved to be the most suitable. The rate of hydrogen produced decreases with time, a behavior that was also seen during chronoamperometry, where the photocurrent showed a pronounced increase until the eighth hour of reaction and then stabilized.

3.5 Mechanism proposal

Studies involving the photocatalytic mechanism of dye degradation by $Bi_2Fe_4O_9$ show that hydroxyl radicals ($^\cdot OH$) are produced on the irradiated $Bi_2Fe_4O_9$, derived mainly from the reaction of the photogenerated holes with water and OH^-, and are scavenged by the addition of an alcohol. For instance, hydroxyl radicals and photogenerated holes are suggested to be
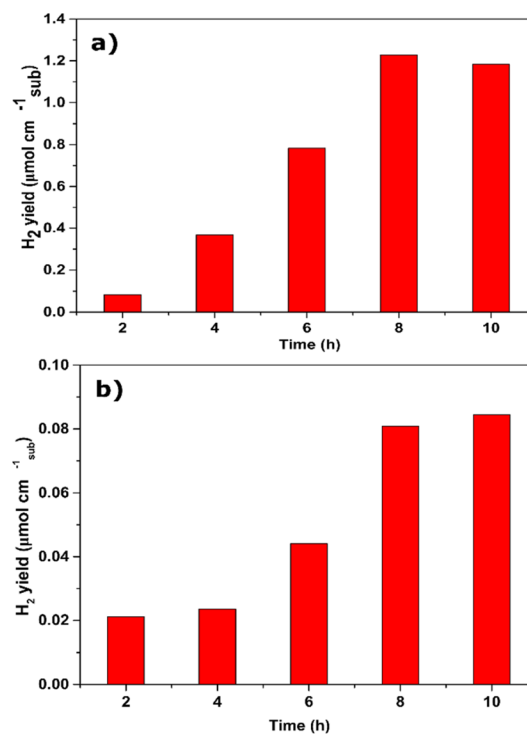

Fig. 5 Hydrogen generated at the Pt foil cathode measured by GC. (a) pH 13.0 and (b) pH 3.5. The hydrogen was collected every two hours during ten hours of experiment.
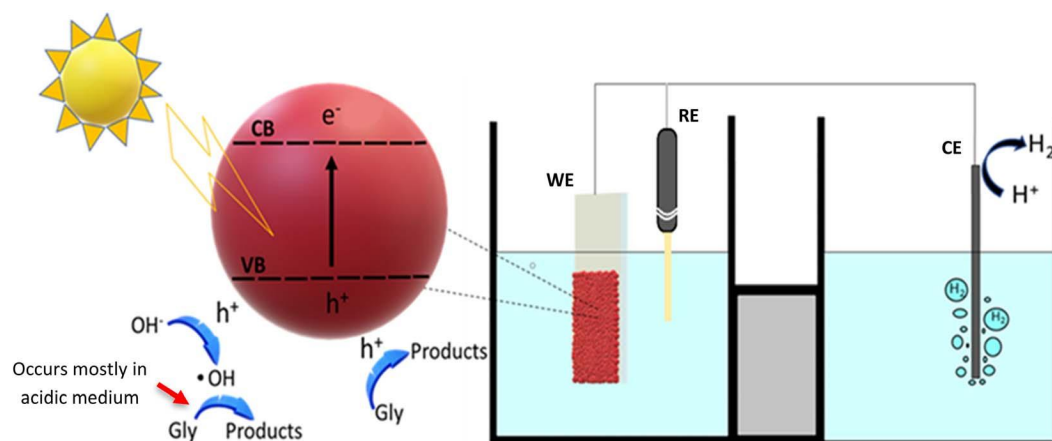
Fig. 6   Sketch of the photoelectrochemical glycerol conversion mechanism using FTO|BFO as the photoanode (WE – Working Electrode), Pt as the cathode (Counter Electrode – CE) and Ag/AgCl as the reference electrode (RE). While holes (h$^+$) are responsible for the GOR in alkaline medium, both hydroxyl radicals and h$^+$ can contribute to the GOR in acidic medium.

the two primary active species involved in the photocatalytic degradation of methylene blue (MB).[41] Furthermore, studies that combine photoluminescence spectroscopy and trapping experiments also show that $\cdot$OH is an active species in the photocatalytic oxidation processes at the $BiFeO_3/Bi_2Fe_4O_9$ heterojunction.[42]

On the other hand, most of the photocatalysts such as α-Fe_2O_3,[43] TiO_2[44] and Ag[45] exhibit negligible $\cdot$OH formation in an alkaline environment, which leads us to believe that the main active species in glycerol oxidation is the photogenerated holes in the alkaline environment, since the activity of $Bi_2Fe_4O_9$ is higher at this pH.

Finally, we clearly show here that the reaction of organic molecules is faster than that of water and that the alkaline media increase the charge separation. Therefore, we hypothesize that the holes generated in alkaline media directly react with the glycerol molecules to form the different products shown in this work. Besides, the higher availability of holes at high pH increases the probability of the oxidation of products/intermediates, generating molecules with higher oxidation degrees and even breaking the C–C chain.

Looking at the photoanode side, both the conduction band and the middle band of $Bi_2Fe_4O_9$ mostly consist of Fe 3d orbitals, while the valence band is mainly composed of oxygen 2p orbitals.[22,33] The excitation of this material by sunlight leaves a hole in the anion valence band, while the electron is promoted to the conduction band (3d-states of Fe).[22,33] A sketch of this mechanism is presented in Fig. 6.

4   Conclusions

To summarize, we have demonstrated the selectivity of BFO photoelectrodes towards glycerol photoelectrooxidation and the possibility of using this photoanode for biomass conversion into value-added chemicals and clean hydrogen. It performed better in alkaline media, exhibiting higher photocurrent at 1.23 V vs. RHE (~4 times higher than that presented at pH 3.5

and ~7 times higher than that presented at pH 5.5) and less recombination and charge transfer resistance. However, at this pH, the reaction selectivity was low, producing 4 different glycerol oxidation products: glycolate, glycerate, lactate and formate.

Despite the low photocurrent at 1.23 V vs. RHE shown at pH 3.5, BFO has been demonstrated to be selective for DHA and glyceraldehyde production, which have a much higher economic value than glycerol. The lowest photocurrent was observed at pH 5.5 and neither glycerol oxidation products nor hydrogen was detected at this pH.

Regardless of the low photocurrents observed, to the best of our knowledge, mullite-type bismuth ferrite has never been used as a photoanode for glycerol photoelectrooxidation. Furthermore, their applications in photoelectrochemistry are very rare, despite presenting desired characteristics of a good photoelectrocatalyst, such as low cost, stability and good absorption.

Like hematite and bismuth vanadate, it will take some time for it to perform at its peak, but in the near future, it may become a promising photoelectrocatalyst candidate. There are several approaches to enhance the performance of BFO, including heterojunction building, morphological modification, doping and nanostructuring. Improvements in the photocurrent and glycerol conversion efficiency may result from these mechanisms. Before moving on to these steps, it is necessary to better understand the properties of this material.

Author contributions

B. L. S. performed BFO photoelectrode synthesis, photoelectrochemical characterization, TAS measurements, chromatographic quantifications and writing process. S. A. C. participated in photoelectrochemical characterization, TAS measurements and writing review. M. B. C. S. participated in HPLC analysis and writing review. L. C. S. participated in photoelectrochemical measurements and writing review. P. S. F.

actively participated in conceptualization, discussion and writing review. C. L participated in discussion and writing review. A. F. N participated in supervision, discussion, funding acquisition and writing review.

Conflicts of interest

There are no conflicts to declare.

Acknowledgements

References

1 L. W. Huang, T. G. Vo and C. Y. Chiang, Converting glycerol aqueous solution to hydrogen energy and dihydroxyacetone by the BiVO4 photoelectrochemical cell, *Electrochim. Acta*, 2019, **322**, 134725.

2 N. Tuleushova, Y. Holade, D. Cornu and S. Tingry, Glycerol electro-reforming in alkaline electrolysis cells for the simultaneous production of value added chemicals and pure hydrogen – Mini-review, *Electrochem. Sci. Adv.*, 2023, **3**(2), e2100174.

3 A. Y. Milanez, G. B. da Silva Maia, D. D. Guimarães and C. L. A. Ferreira, Biodiesel and Renewable Diesel in Brazil: Recent Overview and Perspectives, *BNDES Setorial*, 2022, vol. 28(56), pp. 41–71.

4 D. Liu, J. C. Liu, W. Cai, J. Ma, H. B. Yang, H. Xiao, *et al.*, Selective photoelectrochemical oxidation of glycerol to high value-added dihydroxyacetone, *Nat. Commun.*, 2019, **10**(1), 1779.

5 R. Wang, L. Kou, C. Zhang, X. Zhang, Y. Wang and C. Fan, Single-step synthesis of novel Bi2Fe4O9 nanosheets for high-efficient photocatalytic CO2 reduction to CO, *Mater. Lett.*, 2022, **314**, 131932.

6 T. Li and D. A. Harrington, An Overview of Glycerol Electrooxidation Mechanisms on Pt, Pd and Au, *ChemSusChem*, 2021, **14**(6), 1472–1495.

7 X. Huang, Y. Guo, Y. Zou and J. Jiang, Electrochemical oxidation of glycerol to hydroxypyruvic acid on cobalt (oxy) hydroxide by high-valent cobalt redox centers, *Appl. Catal., B*, 2022, **309**, 121247.

8 H. Liu, L. Li, C. Guo, J. Ning, Y. Zhong and Y. Hu, Thickness-dependent carrier separation in Bi2Fe4O9 nanoplates with enhanced photocatalytic water oxidation, *Chem. Eng. J.*, 2020, **385**, 123929.

9 M. Ma, Y. Chen, Y. Liu, J. Jiang, Z. Jiao and Y. Ma, Highly efficient photocatalytic organic dyes degradation based on 1D magnetic Bi$_2$ Fe$_4$ O$_9$/C@AgBr composite, *Appl. Organomet. Chem.*, 2022, **36**(5), e6619.

10 M. Pooladi, I. Sharifi and M. Behzadipour, A review of the structure, magnetic and electrical properties of bismuth ferrite (Bi$_2$Fe$_4$O$_9$), *Ceram. Int.*, 2020, **46**(11), 18453–18463.

11 Y. Wang, M. Daboczi, C. A. Mesa, S. R. Ratnasingham, J. S. Kim, J. R. Durrant, *et al.*, Bi$_2$ Fe$_4$ O$_9$ thin films as novel visible-light-active photoanodes for solar water splitting, *J. Mater. Chem. A*, 2019, **7**(16), 9537–9541.

12 T. T. Carvalho and P. B. Tavares, Synthesis and thermodynamic stability of multiferroic BiFeO3, *Mater. Lett.*, 2008, **62**(24), 3984–3986.

13 M. Valant, A. K. Axelsson and N. Alford, Peculiarities of a Solid-State Synthesis of Multiferroic Polycrystalline BiFeO3, *Chem. Mater.*, 2007, **19**(22), 5431–5436.

14 C. M. Raghavan, J. W. Kim, S. S. Kim and J. W. Kim, Effect of the annealing temperature on the structural and multiferroic properties of mullite Bi2Fe4O9 thin films, *J. Sol-Gel Sci. Technol.*, 2015, **73**(2), 403–409.

15 F. Gheorghiu, R. Tanasa, M. T. Buscaglia, V. Buscaglia, C. G. Pastravanu, E. Popovici, *et al.*, Preparation of Bi$_2$ Fe$_4$ O$_9$ particles by hydrothermal synthesis and functional properties, *Phase Transitions*, 2013, **86**(7), 726–736.

16 S. Krishna Rao, E. Meher Abhinav, D. Jaison, A. Sundararaj, M. Santhiya, R. Althaf, *et al.*, Investigation of room temperature multi-functional properties of Nd doped mullite Bi2Fe4O9, *Vacuum*, 2020, **172**, 109109.

17 S. Kazhugasalamoorthy, P. Jegatheesan, R. Mohandoss, N. V. Giridharan, B. Karthikeyan, R. J. Josephus, *et al.*, Investigations on the properties of pure and rare earth modified bismuth ferrite ceramics, *J. Alloys Compd.*, 2010, **493**(1–2), 569–572.

18 R. Verma, A. Chauhan, Neha, K. M. Batoo, R. Kumar, M. Hadhi, *et al.*, Effect of calcination temperature on structural and morphological properties of bismuth ferrite nanoparticles, *Ceram. Int.*, 2021, **47**(3), 3680–3691.

19 T. Wu, L. Liu, M. Pi, D. Zhang and S. Chen, Enhanced magnetic and photocatalytic properties of Bi$_2$ Fe$_4$ O$_9$ semiconductor with large exposed (001) surface, *Appl. Surf. Sci.*, 2016, **377**, 253–261.

20 X. Wang, M. Zhang, P. Tian, W. S. Chin and C. M. Zhang, A facile approach to pure-phase Bi2Fe4O9 nanoparticles sensitive to visible light, *Appl. Surf. Sci.*, 2014, **321**, 144–149.

21 H. Idriss, On the wrong assignment of the XPS O1s signal at 531–532 eV attributed to oxygen vacancies in photo- and electro-catalysts for water splitting and other materials applications, *Surf. Sci.*, 2021, **712**, 121894.

22 S. Sun, W. Wang, L. Zhang and M. Shang, Visible Light-Induced Photocatalytic Oxidation of Phenol and Aqueous Ammonia in Flowerlike Bi$_2$ Fe$_4$ O$_9$ Suspensions, *J. Phys. Chem. C*, 2009, **113**(29), 12826–12831.

23 G. Wang, D. Cheng, T. He, Y. Hu, Q. Deng, Y. Mao, *et al.*, Enhanced visible-light responsive photocatalytic activity of Bi25FeO40/Bi2Fe4O9 composites and mechanism investigation, *J. Mater. Sci.: Mater. Electron.*, 2019, **30**(11), 10923–10933.

24 R. P. Antony, M. Zhang, K. Zhou, S. C. J. Loo, J. Barber and L. H. Wong, Synergistic Effect of Porosity and Gradient

Doping in Efficient Solar Water Oxidation of Catalyst-Free Gradient Mo:BiVO$_4$, *ACS Omega*, 2018, **3**(3), 2724–2734.

25 S. Amaral Carminati, A. do Nascimento Barbosa, A. Luiz Martins de Freitas, F. L. Freire, F. L. Souza and A. F. Nogueira, Unraveling the role of single layer graphene as overlayer on hematite photoanodes, *J. Catal.*, 2019, **372**, 109–118.

26 A. E. B. Lima, M. J. S. Costa, R. S. Santos, N. C. Batista, L. S. Cavalcante, E. Longo, *et al.*, Facile preparation of CuWO$_4$ porous films and their photoelectrochemical properties, *Electrochim. Acta*, 2017, **256**, 139–145.

27 Y. Wang, *Effect of Polar Structure on Photocatalytic Properties of Oxide Powders and Films*, 2018.

28 N. Guijarro, T. Lana-Villarreal and R. Gómez, Electron Lifetime in Quantum-Dot-Sensitized Photoanodes by Open-Circuit-Potential Measurements, *ChemPhysChem*, 2012, **13**(16), 3589–3594.

29 M. Barroso, S. R. Pendlebury, A. J. Cowan and J. R. Durrant, Charge carrier trapping, recombination and transfer in hematite (α-Fe2O3) water splitting photoanodes, *Chem. Sci.*, 2013, **4**(7), 2724.

30 A. Yamakata, T. Ishibashi and H. Onishi, Water and Oxygen-Induced Decay Kinetics of Photogenerated Electrons in TiO$_2$ and Pt/TiO$_2$: A Time-Resolved Infrared Absorption Study, *J. Phys. Chem. B*, 2001, **105**(30), 7258–7262.

31 Y. Tamaki, A. Furube, M. Murai, K. Hara, R. Katoh and M. Tachiya, Direct Observation of Reactive Trapped Holes in TiO$_2$ Undergoing Photocatalytic Oxidation of Adsorbed Alcohols: Evaluation of the Reaction Rates and Yields, *J. Am. Chem. Soc.*, 2006, **128**(2), 416–417.

32 S. R. Pendlebury, M. Barroso, A. J. Cowan, K. Sivula, J. Tang, M. Grätzel, *et al.*, Dynamics of photogenerated holes in nanocrystalline α-Fe$_2$O$_3$ electrodes for water oxidation probed by transient absorption spectroscopy, *Chem. Commun.*, 2011, **47**(2), 716–718.

33 Z. Irshad, S. H. Shah, M. A. Rafiq and M. M. Hasan, First principles study of structural, electronic and magnetic properties of ferromagnetic Bi2Fe4O9, *J. Alloys Compd.*, 2015, **624**, 131–136.

34 C. Tang, B. Sun, M. Li, J. Zhang, X. Fan, F. Gao, *et al.*, Surface hydroxylated hematite promotes photoinduced hole transfer for water oxidation, *J. Mater. Chem. A*, 2019, **7**(14), 8050–8054.

35 A. G. Tamirat, J. Rick, A. A. Dubale, W. N. Su and B. J. Hwang, Using hematite for photoelectrochemical water splitting: a review of current progress and challenges, *Nanoscale Horiz.*, 2016, **1**(4), 243–267.

36 S. A. Monny, Z. Wang, T. Lin, P. Chen, B. Luo and L. Wang, Designing efficient Bi$_2$Fe$_4$O$_9$ photoanodes *via* bulk and surface defect engineering, *Chem. Commun.*, 2020, **56**(65), 9376–9379.

37 N. Perini, C. Hessel, J. L. Bott-Neto, C. T. G. V. M. T. Pires, P. S. Fernandez and E. Sitta, Photoelectrochemical oxidation of glycerol on hematite: thermal effects, in situ FTIR and long-term HPLC product analysis, *J. Solid State Electrochem.*, 2021, **25**(3), 1101–1110.

38 M. B. C. de Souza, R. A. Vicente, V. Y. Yukuhiro, C. T. G. V. M. T. Pires, W. Cheuquepán, J. L. Bott-Neto, *et al.*, Bi-modified Pt Electrodes toward Glycerol Electrooxidation in Alkaline Solution: Effects on Activity and Selectivity, *ACS Catal.*, 2019, **9**(6), 5104–5110.

39 Y. Y. Birdja and M. T. M. Koper, The Importance of Cannizzaro-Type Reactions during Electrocatalytic Reduction of Carbon Dioxide, *J. Am. Chem. Soc.*, 2017, **139**(5), 2030–2034.

40 N. Kiratzis, P. Holtappels, C. E. Hatchwell, M. Mogensen and J. T. S. Irvine, Preparation and Characterization of Copper/Yttria Titania Zirconia Cermets for Use as Possible Solid Oxide Fuel Cell Anodes, *Fuel Cells*, 2001, **1**, 211–218.

41 T. Xian, H. Yang, W. Xian, X. F. Chen and J. F. Dai, Photocatalytic mechanism of Bi$_2$Fe$_4$O$_9$ nanoparticles in the degradation of methylene blue, *Prog. React. Kinet. Mech.*, 2013, **38**(4), 417–424.

42 T. Zhang, Y. Shen, Y. Qiu, Y. Liu, R. Xiong, J. Shi, *et al.*, Facial Synthesis and Photoreaction Mechanism of BiFeO$_3$/Bi$_2$Fe$_4$O$_9$ Heterojunction Nanofibers, *ACS Sustain. Chem. Eng.*, 2017, **5**(6), 4630–4636.

43 J. Xu, N. Sahai, C. M. Eggleston and M. A. A. Schoonen, Reactive oxygen species at the oxide/water interface: Formation mechanisms and implications for prebiotic chemistry and the origin of life, *Earth Planet. Sci. Lett.*, 2013, **363**, 156–167.

44 Y. Nakabayashi and Y. Nosaka, The pH dependence of OH radical formation in photo-electrochemical water oxidation with rutile TiO$_2$ single crystals, *Phys. Chem. Chem. Phys.*, 2015, **17**(45), 30570–30576.

45 W. He, Y. T. Zhou, W. G. Wamer, M. D. Boudreau and J. J. Yin, Mechanisms of the pH dependent generation of hydroxyl radicals and oxygen induced by Ag nanoparticles, *Biomaterials*, 2012, **33**(30), 7547–7555.